Rainfall threshold for initiating effective stress decrease and failure in weathered tephra slopes

Max Oke Kluger
M. Ehsan Jorat
Vicki G. Moon
Stefan Kreiter
Willem P. de Lange
Tobias Mörz
Thomas Robertson
David J. Lowe

This is a post-peer-review, pre-copyedit version of an article published in Landslides. The final authenticated version is available online at:
http://dx.doi.org/10.1007/s10346-019-01289-2

RAINFALL THRESHOLD FOR THE BEGINNING OF EFFECTIVE STRESS DECREASE IN WEATHERED TEPHRA SLOPES

Max Oke Kluger[1]*, M. Ehsan Jorat[2], Vicki G. Moon[3], Stefan Kreiter[4], Willem de Lange[5], Tobias Mörz[6], Thomas Robertson[7], David J. Lowe[8]

[1]MARUM – Research Faculty, University of Bremen, Leobener Straße 8, 28359 Bremen, Germany, Orcid:0000-0001-9130-8948

[2]School of Applied Sciences, Abertay University, Dundee, DD11HG, United Kingdom, Orcid: 0000-0001-6972-5921

[3]School of Science, University of Waikato, Hamilton, New Zealand, Orcid:0000-0001-7378-8490

[4]MARUM – Research Faculty, University of Bremen, Leobener Straße 8, 28359 Bremen, Germany, Orcid:0000-0002-1110-7765

[5]School of Science, University of Waikato, Hamilton, New Zealand, Orcid: 0000-0002-6467-0308

[6]MARUM – Research Faculty, University of Bremen, Leobener Straße 8, 28359 Bremen, Germany, Orcid:0000-0002-6865-7864

[7]School of Science, University of Waikato, Hamilton, New Zealand

[8]School of Science, University of Waikato, Hamilton, New Zealand, Orcid: 0000-0002-2547-6019

*Corresponding author, Email: mkluger@marum.de

Abstract

Rainfall is one of the most important triggers of slope failure. Altered pyroclastic (tephra) deposits are especially vulnerable to slope failure because they commonly form slopes of high porosity and high clay content. Empirically-derived thresholds for the triggering of landslides are commonly based on rainfall conditions and have been widely applied in volcanic soils. However, so far only few researchers utilized pore water pressure in the slope as additional variable for the threshold calibration. Here we derived a new rainfall threshold for the beginning of effective stress decrease in the slope by analyzing a long-term record of rainfall and piezometer data from a slide-prone coastal area in northern New Zealand that consists of clayey, halloysitic tephra deposits. We further found that rainfall events that triggered landslides during the investigation period were well constraint by the global rainfall intensity-duration threshold of Sidle and Ochiai (2006) and the local rainfall duration threshold by Wei et al. (2018). We observed the highest effective stress decrease during the rainfall events that caused landslides. Therefore, the new effective stress threshold may be a beneficial contribution to better predict rainfall induced landslides in the future.

Keywords landslides; rainfall threshold; altered tephra; spheroidal halloysite; rainfall-induced slope failure; rotational landslides

1. INTRODUCTION

Rainfall-induced landslides occur globally in all types of environments, posing a major natural hazard to people and infrastructure. Coastal environments are especially vulnerable to landslides because they often exist of highly populated terrain with steep slopes (Agostini et al., 2014; Assier-Rzadkieaicz et al., 2000; Longva et al., 2003; Rösner, 2016). The severity of landslides is further controlled by the presence of sensitive soils in the slope. The special role of sensitive soils is their pronounced post-failure softening behavior, which may lead to progressive landslides with long runout distance difficult to predict (Demers et al., 2014; Kvalstad et al., 2005; L'Heureux et al., 2014). Tephra deposits, encompassing all pyroclastic materials of any grain size (Lowe, 2011), are highly susceptible to slope failure and responsible for catastrophic landslides (Chigira, 2014; Sidle and Ochiai, 2006). Halloysite is a common weathering product of rhyolitic (silica-rich) tephra (Churchman and Lowe, 2012) and has been found to dominate slide surfaces of rainfall-induced landslides in Hong Kong, Japan, New Zealand, Hawaii, and the conterminous United States (Chigira, 2014; Chigira and Yokoyama, 2005; Irfan, 1992, 1998; Kirk et al., 1997; Kluger et al., 2017; Parry et al., 2000, 2001; Shaller et al., 2016; Taskey, 1977; Wen and Aydin, 2003; Yamao et al., 2016). Halloysite is known to form low-permeability soils with high sensitivity (Kluger et al., 2017; Moon et al., 2015b; Smalley et al., 1980). Reviews by, e.g., Chigira (2014) highlighted the importance of better understanding the triggering mechanisms and landslides dimensions in halloysitic soils.

The most important trigger of landslides is effective stress decrease due to rainfall-induced excess pore water pressure in the slope. Rainfall thresholds are widely used to forecast the likely occurrence of landslides by defining the minimum rainfall necessary to trigger landslides (Segoni et al., 2018a). Caine (1980) developed a first global rainfall threshold, which links rainfall intensity and duration to the occurrence of landslides by means of a simple power law function. Since then, a large variety of rainfall thresholds have been derived at different scales (global, regional, local), by using different rainfall parameters, and for different types of landslides (Guzzetti et al., 2007, 2008; Segoni et al., 2018a). In their recent review, Segoni et al. (2018a) summarized that most rainfall thresholds are derived for shallow landslides and debris flows, whereas only few studied rainfall thresholds for deep-seated landslides, rockslides, and earthflows. Furthermore, Segoni et al. (2018a) recognized that most studies solely rely on rainfall data when calibrating rainfall thresholds and found only two case studies (Baum and Godt, 2010; Napolitano et al., 2016) in which pore water pressure data provided additional insight into the triggering of landslides. Knowledge about pore water pressure is useful to calculate the change in effective stress in the soil slope due to rainfall (Duncan et al., 2014) and would therefore add a new beneficial perspective in the determination of rainfall thresholds (Segoni et al., 2018a).

Our study area is the Omokoroa Peninsula (Omokoroa hereafter), located in the central part of Tauranga Harbour, New Zealand's largest barrier-enclosed estuarine lagoon (Fig. 1A-B). Omokoroa's geology

consists mainly of a thick succession of Quaternary-aged rhyolitic tephra-fall deposits derived largely from eruptions in the Taupo Volcanic Zone, together with intercalated paleosols, underlain by ignimbrite (Briggs et al., 2005). One specific composite unit within the siliceous tephra succession, the Pahoia Tephra sequence (Pahoia Tephras hereafter), has been highly altered to form clay-rich deposits dominated by halloysite and has very high sensitivities (Kluger et al., 2017; Smalley et al., 1980). These highly sensitive Pahoia Tephras were involved in the deep-seated Bramley Drive landslide, located on the northwest coast of Omokoroa (Kluger et al., 2017; Moon et al., 2015b). The main failure occurred in 1979 CE after prolonged heavy rainfall and was reactivated by smaller retrogressive failures in 2011, and 2012. The Pahoia Tephras, acting as an aquiclude as well as sliding material, were transported over long runout distances into Tauranga Harbour. During two rainfall events associated to cyclones Debbie and Cook in 2017, 27 new landslides occurred along the coast of Omokoroa causing damage to numerous houses and properties (Tab. 1C-E). This study area is therefore ideal for investigating triggering mechanisms and landslide dimensions of rainfall-induced landslides in sensitive halloysitic tephras, and demonstrably important also for informing landslide hazard analysis and potential mitigation (Basher, 2013; Crozier, 2005).

In this study, we used field observations including mapping, and a combination of bathymetry and seismic data, to identify the failure dimensions and geological preconditioning factors of the landslides at Omokoroa. We then compare these features with those of landslides in various material types and environments worldwide. By analyzing 4.5 years of rainfall and pore water pressure data recorded at the Bramley Drive landslide since 2014, we calibrate and validate empirical rainfall thresholds for the occurrence of landslides and for the beginning of effective stress decrease in the slope.

2. GEOLOGICAL SETTING

The Tauranga basin extends along the Bay of Plenty coastline, in the northeastern part of New Zealand's North Island (Briggs et al., 1996) (Fig. 1B). The Waiteariki Ignimbrite, deposited c. 2.09 Ma (Briggs et al., 2005), forms the local basement. Its eruption initiated a period of rapid subsidence (Houghton and Cuthbertson, 1989). The ensuing basin was infilled in part by volcanogenic sediments, ignimbrites and silica-rich tephra-fall deposits originating initially from eruptions in the Coromandel Volcanic Zone and then the Taupo volcanic zone. The post-glacial marine transgression (attaining near-modern sea level c. 7,500 years ago), which followed the lowered sea level associated with the Last Glacial Maximum, formed a large barrier-enclosed mesotidal estuarine lagoon, the Tauranga Harbour (Briggs et al., 1996). The lagoon is blocked from the sea by two tombolos at Bowentown and Mt Maunganui, and the diachronous Pleistocene and Holocene barrier island of Matakana Island (Shepherd et al., 2000). Most of the lagoon comprises extensive estuaries and mudflats that are exposed at low tides. A number of terraces extend into Tauranga Harbour as northeast- to north-northeast-trending peninsulas, which commonly have near-level surfaces 20 to 40 m above sea level and steep slopes or cliffs on their coasts that are prone to landslides (Briggs et al., 1996; Chappell, 1975).

One of these peninsulas is that at Omokoroa (Fig. 1A), which has experienced numerous coastal landslides (Fig. 1C-E). Omokoroa comprises a ~40-m-thick succession of mainly Quaternary rhyolitic tephras (Fig. 2A): the Pahoia Tephra sequence includes (from base to top) lignite, paleosol P1, unwelded pumiceous deposits of the Te Puna Ignimbrite (c. 0.93 Ma), and a series of altered clay-rich halloysitic tephra beds, which are divided into lower and upper Pahoia Tephras based on two distinct paleosols P2 and P4. All of these deposits and intercalated paleosols are overlain by successions of younger, strongly-altered tephras called Hamilton Ashes (c. 0.35 to c. 0.05 Ma) and late Quaternary tephras (≤ c. 0.05 Ma). Apart from the near-surface late Quaternary tephras (which are mainly allophanic), the tephras have been altered to halloysites with different morphologies, ranging from mainly tubular in the Hamilton Ashes and Upper Pahoia Tephras, to mainly spheroids in the lower Pahoia Tephras, and to mainly polyhedrons and books in the Te Puna Ignimbrite (Cunningham et al., 2016; Kluger et al., 2017). The lower Pahoia Tephras include the highly sensitive halloysitic layer that was involved in the failure of the 1979 Bramley Drive landslide (Fig. 2B-C). Kluger et al. (2017) reported a new mushroom cap-shaped variety of the spheroidal halloysite morphology (Fig. 2D), which, through its surface-charge characteristics, causes the layer to be highly sensitive and thus contributes to the landslide susceptibility at Omokoroa. The highly sensitive halloysitic layer is porous (Smalley et al., 1980), but has also low permeability (Moon et al., 2015b), affecting the hydrogeology of the tephra successions at Omokoroa. Based on piezometer recordings at the Bramley Drive landslide, an aquiclude located in the lower Pahoia Tephras prohibits downward directed drainage of rainwater, while an overlying aquifer provides sufficient drainage to cause fluctuation of the effective stresses in the slope (Moon et al., 2015a).

3. MATERIALS AND METHODS

3.1. Landslide characterization

The landslides that occurred at Omokoroa's coast since the 1979 Bramley Drive landslide were characterized according to material composition, type, volume, and travel angle. We performed a detailed landslide survey after the 2017 cyclone season in April 2017. The survey included the following steps. The lithological compositions of the slides were identified by descriptions of samples taken from the landslide scarp and slide debris, or alternatively through observation of exposed scarp faces and correlations to the known regional stratigraphy at Omokoroa. The landslides were classified according to Cruden and Varnes (1996) being either deep-seated (with rotational slip surface), shallow or composite earth slides. The composite earth slides always resulted from both deep-seated and shallow failures and are hereafter attributed to the deep-seated and shallow earth slides on the basis of the dominant mode of failure. The decision about which mode of failure dominated the landslide was made by the authors'

expert judgements. We calculated volumes of deep-seated landslides V_{ds} by assuming the slip surfaces followed the shape of half an ellipsoid with semiaxes D_s, $W_s/2$, and L_s (Cruden and Varnes, 1996):

$$V_{ds} = \frac{1}{6}\pi D_s \cdot W_s \cdot L_s \tag{1}$$

Where L_s is the distance from toe of slip surface to crown of the main scarp. W_s is the maximum width between flanks of the landslide perpendicular to L_s. D_s is the maximum depth of the slip surface below original ground surface, measured perpendicular to the plane containing W_s and L_s. The orientation of the original ground surface was derived from a 1-m-resolution LIDAR digital elevation model of Omokoroa, which was recorded before the landslides in 2015. It is widely accepted practice to estimate volumes of shallow landslides V_s from landslide area A_L and two empirically derived parameters, the scaling exponent c and intercept a (Guzzetti et al., 2009; Larsen et al., 2010; Malamud et al., 2004).

$$V_s = aA_L^c \tag{2}$$

$$A_L = W_s \cdot L_s \tag{3}$$

In our study we used a scaling exponent of $c = 1.332$ and an intercept of $log a = -0.836$ to estimate volumes of shallow landslides. These values are derived from an international data base of soil landslides (Larsen et al., 2010). The travel angle β of landslides is calculated following Cruden and Varnes (1996) as

$$tan\beta = H/L \tag{4}$$

$$\beta = \tan\left(\frac{H}{L}\right)^{-1} \tag{5}$$

Where H/L is the height-to-length ratio (Cruden and Varnes, 1996), which is calculated from the vertical H and horizontal distances L between the crown and the tip of the landslide, respectively. The volume and travel angle of the 1979 Bramley Drive landslide were estimated from Gulliver and Houghton (1980).

We further studied the volumes and travel angles of historical landslides that occurred at Omokoroa in the past by surveying the geological record of the sediments deposited in the subtidal area close to Omokoroa's coast. By using a $200/400$ kHz shallow water multibeam echosounder (Reson Seabat 7125) onboard vessel *Pandora*, and a 3.5 kHz seismic system (Knudsen Pinger CHIRP SBP) mounted on the vessel *Tai Rangahau*, we mapped the seafloor morphology and sedimentary subsurface structures of potential remnant landslide deposits. The bathymetric and seismic data cover an elongated northeast trending area c. 1,300 m long and c. 250 m wide (Fig. 1A). The bathymetric data have a grid resolution of 1 m by 1 m and the seismic data form a grid of approximately parallel profiles with c. 50 m spacing.

3.2. Evaluation of rainfall and pore water pressure

We consider our study area at Omokoroa to be of local scale, with maximal length of 1,800 m, maximal width of 300 m, and an area of c. 0.5 km^2. Rainfall that occurred from January 2014 to June 2018 was therefore recorded by a single tipping bucket rain gauge (Ogawa Seiki Co.) located close to the Bramley Drive landslide (Fig. 1A) (Moon et al., 2015a). According to Segoni et al. (2018a) a rain gauge density of 200 per 100 km^2, as used in our study, is within the middle range considered in recent studies about rainfall thresholds. The maximal distance between the rain gauge and landslides was c. 1000 m. The rain gauge at the Bramley Drive landslide exhibited time periods with data gaps (Fig. 3B). We therefore supplemented the missing record with rainfall data collected from the nearest rain gauge at Goodall Road, Whakamarama, being located c. 6.5 km SW of Omokoroa (Fig. 1B). Because rainfall within Tauranga Harbour has been observed to be variable (Quayle, 1984), we confirmed the accordance between both rainfall regimes by statistical correlation (Fig. 3C-D). For this purpose, we identified rainfall events that were recorded by both rain gauges and found that cumulated rainfall and rainfall duration at the Bramley Drive landslide are both well represented by the rain gauge at Goodall Road, Whakamarama. The sampling rates for the rainfall gauges were every 10 minutes at the Bramley Drive landslide and every 60 minutes at Goodall Road, Whakamarama. Because of that we resampled the rainfall data of both stations to hourly rainfall.

Pore water pressure changes were recorded every 10 minutes from January 2014 to June 2018 by three piezometers (Glötzl PP-3). The piezometers have been installed in a borehole close to the rain gauge of the Bramley Drive landslide at depths of 12, 21, and 27.5 m (Moon et al., 2015a). The depths were chosen to record the pore water pressure in the aquifer (above and below the mean ground water level) and in the confined aquifer below the aquiclude and are hereafter referred to as upper, middle, and lower piezometers, respectively (Fig. 2C). Due to technical issues, the piezometers did not record any data from March to July 2016 (indicated by 'data gap' in Fig. 3A).

We analyzed the rainfall and piezometer data to relate rainfall parameters (cumulated rainfall, rainfall intensity, and duration) of individual rainfall events to pore water pressure increase and to the triggering of landslides. The extraction of rainfall parameters from the pluviograph and the separation of individual rainfall events was based on defining a standard time period without rainfall. The duration of dry periods commonly chosen for separating individual rainfall events varies from six hours (Tiranti and Rabuffetti, 2010) to four days (Brunetti et al., 2010). In our study, the pore water pressure from rainfall dissipated within a couple of hours after the rainfall stopped and never exceeded six hours (Fig. 3E). Therefore, we defined an individual rainfall event as continuous rainfall being separated from the next rainfall event

by a dry period of at least six hours following the suggestions made by Tiranti and Rabuffetti (2010). For each rainfall event, we calculated the cumulated rainfall, duration, and rainfall intensity. We classified the rainfall events that caused an increase in pore water pressure in at least one of the piezometers as 'large rainfall events', and those with no impact on the pore water pressure as 'small rainfall events.' Destabilization of the soil slope because of large rainfall events was assessed by considering the decrease in effective stress due to pore water pressure. The effective stress σ' was calculated as:

$$\sigma' = \sigma - u \tag{6}$$

where σ is the total overburden stress, which we estimated from long-spaced gamma density logging in the slope of the Bramley Drive landslide (Kluger et al., 2018), and u is the pore water pressure measured by the piezometers.

All 27 landslides since January 2014 were observed shortly after two large rainfall events during cyclones Debbie and Cook in 2017. The timings of these landslides were solely based on eye witness reports of residents living close to the coast of Omokoroa, yielding a temporal resolution of landslide occurrence of 1 day. The attribution of rainfall events to the triggering of landslides was therefore performed manually, without any measurement of soil displacement during landslides or the like. Because of the low number of rainfall events (N=2) that triggered landslides, we did not derive own rainfall thresholds for the occurrence of landslides, but compared the two large rainfall events during cyclones Debbie and Cook that triggered landslides at Omokoroa to the global rainfall intensity-duration threshold suggested by Caine (1980), which was later updated by Sidle and Ochiai (2006) (Eq. 7).

$$I = \alpha D^{-\gamma} \tag{7}$$

Where I is the rainfall intensity (mm/h), D is the duration of rainfall (h), and $\alpha = 13.58$ and $\gamma = 0.38$ are the intercept and slope of the power law function, respectively. Additionally, we adopted the Frequentist method to statistically analyze rainfall events that caused an effective stress decrease (i.e. large rainfall events) and calibrated a rainfall intensity-duration threshold for the beginning of effective stress decrease. The Frequentist method was first described by Brunetti et al. (2010) and has since been applied in several study areas in Italy (Peruccacci et al., 2012; Segoni et al., 2018a). Following Brunetti et al. (2010), we applied frequency analysis on the large rainfall events and calibrated a rainfall threshold (Eq. 7) for the beginning of effective stress decrease at the 5% confidence interval. Assuming the catalogue of large rainfall events sufficiently represents the rainfall conditions at Omokoroa, we can state that the probability of effective stress decrease by rainfall below this threshold is less than 5% (Brunetti et al., 2010).

We validated the predictive capability of the global rainfall threshold by Sidle and Ochiai (2006) and our new effective stress threshold by compiling contingency matrices (one for each threshold) that classify rainfall events as either true positives (TP), true negatives (TN), false positives (FP), or false negatives (FN) (Tab. 2). The validation was performed using the entire data set of rainfall events between January 2014 and June 2018. The contingency matrices were used to calculate different skill scores (sensitivity, specificity, positive prediction power, negative prediction power), which are common statistical parameters to evaluate predictive capability (Martelloni et al., 2012; Rosi et al., 2015; Segoni et al., 2018a).

4. COASTAL LANDSLIDES IN HALLOYSITIC TEPHRA DEPOSITS

4.1. Preconditioning factors

A large number of landslides occurred along the northwest coast of Omokoroa as consequence of two large rainfall events during cyclones Debbie and Cook in 2017. We counted a total of 27 coastal landslides and overlaid the topography in Fig. 1A with our mapping results of main scarps and dimensions of landslide deposits. The landslides, having an average spacing distance of 80 m between each other, affected the highly populated coastal residential area of Omokoroa (Fig. 1C-E). The majority of landslides resulted from shallow slope-parallel failures within the upper unwelded pumice layers of the Te Puna Ignimbrite and overlying halloysitic tephra deposits of the Pahoia Tephras (c.f. Fig. 1C, Tab. 1). Shallow landslides occur occasionally along the entire coastline and become dominant at the eastern coast along Myrtle Drive and Crapp Reserve.

We counted ten deep-seated landslides. One of these, the McDonnell Str landslide (L-9), followed a similar failure and sliding mechanism than the 1979 Bramley Drive landslide (L-11). Both landslides, depicted in Figs. 1D-E, resulted from an initial rotational failure that reached into the highly sensitive lower Pahoia Tephras. The landslide masses then eroded the upper parts of the Te Puna Ignimbrite until they reach sea level and formed flow slides into the lagoon of Tauranga Harbour. The benches of the initial rotational failures are highlighted by white dashed lines in Figs. 1-D-E. The other deep-seated landslides resulted from rotational failures, which were sometimes associated with minor shallow slides.

Preconditioning factors for landslides have been widely discussed in the literature (Cruden and Varnes, 1996; Duncan et al., 2014; Varnes, 1978). We consider that the most important preconditioning factors for the coastal landslides at Omokoroa lie in a combination of low permeability, being in the order of $5 \cdot 10^{-10}\, m/s$, and high sensitivity of the halloysitic tephra layers within the lower Pahoia Tephras (Kluger et al., 2018; Kluger et al., 2017; Moon et al., 2015b). Low-permeability clay layers interbedded in soil slopes can occur in all types of deposits and environments worldwide and these situations probably represent the most intensely studied preconditioning factor for pore water pressure-induced landslides (Zaruba and Mencl, 2014). Regardless of the mineralogy of the clay layers, their low-permeability

effected the water infiltration into the slope, therefore affecting pore water pressure in the overlying aquifer. Following the effective stress principle (Eq. 3) and the Mohr-Coulomb failure theory, an increase in pore water pressure causes a reduction in effective stress, and hence a reduction in shear strength (Labuz and Zang, 2012). Where pore water pressure reduces the shear strength of the slope material to a critical level, landslides are triggered.

Sensitivity is the ratio of maximum shear strength to post-failure residual shear strength, where a value of more than 30 is defined as highly sensitive (Norsk Geoteknisk Forening, 1974; Skempton and Northey, 1952). Kluger et al. (2017) studied the relationship between halloysite clay morphology and sensitivity in intact tephras from the Bramley Drive landslide and measured the highest sensitivities of $S = 55$ in mushroom cap-shaped (MCS) spheroidal halloysite, whereas sensitivity development was lower ($S \leq 10$) in tubular halloysite. The MCS spheroidal halloysite is most abundant in the lower Pahoia Tephras, which have been involved in the failure of the 1979 Bramley Drive landslide (Figs. 1E and 2). Our observations of the compositions of the slide material show that some of the deep-seated landslides initially failed within the lower Pahoia Tephras. Furthermore, a number of shallow-translational landslides also involved failure within the Pahoia Tephras. These observations highlight the special role of spheroidal halloysite in landslides at Omokoroa. Similar observations have also been reported in Japan, where 'ball-shaped' halloysite was associated with slip surfaces in altered tephras (Tanaka, 1992).

Spheroidal halloysite is commonly formed by rapid precipitation from silicon-rich and aluminum-bearing solutions derived from the dissolution of volcanic glass shards and primary mineral grains (Cravero and Churchman, 2016; Joussein et al., 2005). Researchers have reported the occurrence of spheroidal halloysites in cold to tropical regions around the world within various volcanogenic host materials of rhyolitic, andesitic, and basaltic composition (Adamo et al., 2001; Askenasy et al., 1973; Birrell et al., 1955; De Oliveira et al., 2007; Jeong and Kim, 1996; Kirkman, 1977; Loughnan and Roberts, 1981; Parham, 1970; Quantin and Rambaud, 1987; Romero et al., 1992; Saigusa et al., 1978; Sieffermann and Millot, 1969; Singer et al., 2004; Wada and Kakuto, 1985). Furthermore, neoformation of spheroidal halloysite was also observed in tephra layers offshore from Sumatra and Peru (Imbert and Desprairies, 1987; Pouclet et al., 1990). This global occurrence shows the importance of better understanding the role of spheroidal halloysite in sensitivity development and its role in preconditioning large landslides with a progressive failure mechanism.

4.2. Landslide dimensions

We evaluated the dimensions of the landslides that have occurred along the coast of Omokoroa since 1979 (Fig. 4). The majority of landslide are of relatively small volumes, ranging between 100 and 4,500 m^3, and steep travel angles between 17° and 60° (Tab. 1). Notable exceptions are the McDonnell Str landslide (L-9) and the 1979 Bramley Drive landslide (L-11), having volumes of c. 11,000 and 60,000 m^3 and travel angles of 15° and 9°, respectively. The travel angles of landslides observed in our study linearly decrease (in log-log scale) with landslide volume, indicating longer runout distances. We observed that deep-seated landslides generally exhibited higher volumes and lower travel angles than shallow landslides, but that both landslide types follow the same volume-to-travel angle relationship (c.f power law fit (a) in Fig. 4).

The coastal erosion of the peninsulas within Tauranga Harbour, ensuing after the post-glacial transgression, was likely to be accompanied by different forms of mass wasting, such as landslides. Therefore, we posit that studying the record of nearshore sediments will enable us to recognize dimensions of landslides that occurred along Omokoroa's coast in the past. The seismic and bathymetry data cover the subtidal nearshore area off northwest Omokoroa and provide a three-dimensional view of four sedimentary units (Units 1 to 4) identified within the upper 15 m below the sea surface (Figs. 1A and 5). The basal Unit 1 is characterized by high impedance with little internal structure. The upper boundary of Unit 1 is defined by an undulating reflector having several peaks that are commonly separated by terraced troughs. The overlying Unit 2a is internally characterized by numerous reflectors of varying orientation. We identified a channel-like structure within this unit (Unit 2b) with cross-bedded reflectors. The overlying Unit 3a truncates the top reflector and some of the internal inclined reflectors of the channel-like Unit 2b. Unit 3b truncates Units 2a, 2b, and 3a. Both truncating units are of low impedance. Unit 3a exhibits some poorly defined chaotic internal reflectors with preferred inclination towards the northwest, whereas Unit 3b is horizontally oriented without any internal reflectors. Units 2 and 3 are overlain by a thin slope-parallel unit (Unit 4), which is recognizable in the shallow southeast area.

We interpret the basal Unit 1 to be the local basement consisting of the Waiteariki Ignimbrite. Unit 2 represents estuarine and fluvial volcanogenic sediments of mainly volcanogenic origin from the eroded Waiteariki Ignimbrite and newer ignimbrites and multiple tephra-fall deposits, such as the Te Puna Ignimbrite and Pahoia Tephras, respectively. The younger Units 3a and 3b are erosive by nature and exhibit either chaotic internal reflectors or no reflector at all. We therefore interpret them to be deposits of two major pre-historic landslide events that occurred at Omokoroa at the end of the post-glacial transgression when the coastline of Omokoroa was located close to that of the present day.

Given the close proximity to Omokoroa, it is possible that the pre-historic landslide deposits are composed of sensitive halloysitic tephra materials originating from the lower Pahoia Tephras. This interpretation is supported by the findings of Jorat et al. (2017), who identified Pahoia Tephra landslide deposits in the eastern part of Tauranga Harbour. The slope-parallel layer (Unit 4) only occurs slightly below the intertidal zone and is therefore likely composed of sediments influenced by tides and/or storm waves. We suggest that the second pre-historic landslide deposits (Unit 3b) in the subtidal area off Omokoroa

followed a similar sliding mechanism to the two deep-seated failures with associated flow slides (L-9 and L-11). We therefore interpolated the extent of the second pre-historic landslide deposits within the seismic profiles and superimposed the associated thickness and maximum extent on Fig. 1A. The interpolated thickness of the second pre-historic landslide averages between 0.5 and 1.5 m. The interpolated thickness of the second pre-historic landslide is limited to a small area of the assumed landslide area and therefore provides only a rough estimate of the original landslide thickness. Assuming some major tidal erosion of the landslide to have taken place after deposition, we consider a constant layer thickness of 1 m to be the lower limit bounding the original landslide. The area enclosed by the line of maximum extent and the present-day coastline of Omokoroa is c. 185,000 m^2 and, together with an assumed cliff height of $H = 35$ m and a maximal runout distance of $L = 360$ m, results in a landslide volume of 185,000 m^3 and a travel angle of $\beta = 5.5°$.

The volume-to-travel angle relationship of the landslides at Omokoroa are similar to those of other landslides in halloysitic tephras from Japan and Hong Kong (Chigira et al., 2013; Irfan, 1992; Kirk et al., 1997; Wang et al., 2014) (Fig. 4), highlighting the applicability of our study to locations beyond New Zealand. We further compared dimensions of landslides in halloysitic tephra deposits with those in other environments worldwide. When considering landslides with similar volume (e.g. $V = 10^6$ m^3), subaerial landslides commonly exhibit higher travel angles, whereas submarine landslides and quick clay landslides are known to have smaller travel angles than landslides in halloysitic soil (Edgers and Karlsrud, 1982; Hampton et al., 1996; Hsu, 1975; L'Heureux et al., 2012; Nicoletti and Sorriso-Valvo, 1991; Scheidegger, 1973). The comparison with other environments illustrates that landslides in halloysitic soil exhibit travel angles between subaerial and submarine landslides. For Omokoroa we can interpret this with the fact that the landslides occurred at the interface between terrestrial and marine environment and that the fluidization commonly observed in submarine slides (Hampton et al., 1996) may have taken place in our study area to limited extent.

5. RAINFALL THRESHOLD FOR HALLOYSITIC TEPHRA DEPOSITS

5.1. Rainfall-induced pore water pressure increase

We analyzed the pore water pressure increase to rainfall in order to better understand the trigger mechanisms of rainfall-induced landslides in halloysitic tephras. The low-permeability tephras (including the highly sensitive layer) in the lower Pahoia Tephras act as a water infiltration barrier, creating an overlying unconfined aquifer and an underlying confined aquifer in the slope at Bramley Drive (Fig. 2C). Based on data from the middle piezometer, the water table in the overlying unconfined aquifer is located at an average depth of around 15 m and it exhibits small seasonal but no long-term annual variations (Fig. 3A). The pore water pressure in the unconfined aquifer responds to rainfall events in distinctive spikes, which commonly decay towards background levels within minutes to hours (Fig. 3A and E). We link the distinctive spikes to direct stress transfer from rainwater that infiltrates the partly saturated soil slope above the aquifer. Sometimes the distinctive spikes are followed by smaller pore water pressure increase with longer decay time, which may reflect a temporary rainfall-induced change in gradient of the regional hydraulic head. These smaller pore water pressure increases with longer decay time were not further considered in this study. Based on observations of the lower piezometer, the confined aquifer exhibits small overall variations in pore water pressure, which sometimes mimic the seasonal variations and pore water pressure increases with longer decay time observed in the unconfined aquifer (cf. examples 1 and 2 in Fig. 3A). Except for two minor spikes in 2014, we did not observe any pore water pressure increase that resulted from direct rainwater infiltration into the confined aquifer. This lack of direct increase indicates that the confined aquifer exhibits some connections to the regional hydrogeological system, but is not in direct contact with the unconfined aquifer.

We enumerated 816 rainfall events within the evaluation period of 4.5 years. Of those, we identified 41 large rainfall events, which caused a direct pore water pressure increase in the unconfined aquifer at Bramley Drive (Fig. 3A-B). Some rainfall data of the large rainfall events are taken from the nearest rain gauge at Goodall Road, Whakamarama (cf. light green circles in Fig. 5B).

We observed some of the largest rainfall events with strong pore water pressure increase during the 2017 cyclone season from March to April 2017 (Fig. 3E). The rainfall events cluster in four groups at intervals of one to two weeks and accumulated a total rainfall of more than 800 mm. The pore water pressure increase recorded during the third and fourth group of rainfall events, namely cyclones Debbie and Cook, rank among the highest recorded during the investigation period, and ultimately triggered all 25 landslides that occurred at Omokoroa since 2014. We therefore conclude that rainfall and pore water pressure measured at the Bramley Drive landslide are characteristic for the other locations of landslides that occurred across the entire northwest coast of Omokoroa.

5.2. Rainfall thresholds

We analyzed the rainfall events in order to better understand the role of rainfall intensity and duration in the triggering of landslides and in the beginning of effective stress decrease. For this purpose, we plotted the water tables of small rainfall events with respect to rainfall intensity and duration (grey circles in Fig. 6). We overlaid the small rainfall events with vertical arrows indicating an increase in water table due to large rainfall events. In addition to the change in water table due to rainfall, we considered the decrease in effective stress in the lower Pahoia Tephras as indicator for strength loss in the soil slope. Small rainfall events do not induce any pore water pressure in the unconfined aquifer. The pore water pressure measured at the middle piezometer during the small rainfall events therefore forms a satisfactory statistical basis for calculating the background effective stress level within the lower Pahoia Tephras. From long-spaced gamma density logging in the slope of the Bramley Drive landslide (Kluger et al., 2018), and our long-term piezometer record during small rainfall events, we calculated a total

overburden stress of $\sigma = 337$ kPa and a pore water pressure of $u = 65 \pm 5$ kPa, which yielded a background effective stress of $\sigma_b' = 272 \pm 5$ kPa at the middle piezometer (Eq. 6) (cf. Fig. 6B).

Large rainfall events temporarily reduce the effective stress in the lower Pahoia Tephras to different extent depending on rainfall intensity and duration. The effective stress began to decrease when rainfall intensities exceeded 2 mm/h at durations of more than 2.5 h. The largest effective stress decreases occurred only when rainfall intensities exceeded 4 mm/h at durations of more than 4 h. The large rainfall events during cyclones Debbie and Cook, preceding the landslides at Omokoroa, caused the highest and third-highest effective stress decrease within the studied time period. They exhibited remarkably long durations of c. 25 h at moderate rainfall intensities of 4 mm/h. The large June 2018 rainfall event (as highlighted in Fig. 6B), causing the second-highest effective stress decrease, was not associated with any landslide event. In comparison to the rainfall events during cyclones Debbie and Cook, the June 2018 rainfall event exhibits higher rainfall intensity, but at shorter duration of c. 16 h. These observations indicate that in our study area a duration of rainfall between 16 and 25 h possibly represents a critical level for landslide triggering. This finding is in accordance with those of Wei et al. (2018), who related shallow landslides in Taiwan to rainfall events having durations of more than 24 h.

Rainfall thresholds are widely used to forecast the likely occurrence of landslides (Guzzetti et al., 2007, 2008; Segoni et al., 2018a). We compared our two rainfall events that triggered landslides since January 2014 with the global rainfall intensity-duration threshold by Sidle and Ochiai (2006) (Eq. 7) and with a regional rainfall duration threshold by Wei et al. (2018). For this purpose, we displayed the rainfall intensities and durations of all rainfall events that triggered and that did not trigger landslides together with the two rainfall thresholds by means of logarithmic and linear scales (Fig. 7). The two rainfall events that triggered landslides are well constraint by both rainfall thresholds.

The influence of rainfall intensity and duration on effective stress decrease was further studied by introducing a normalized effective stress decrease $\Delta\sigma_N'$ (in percentage), which quantifies the decrease in effective stress from the background effective stress due to large rainfall events (Eq. 8)

$$\Delta\sigma_N' = \left(1 - \frac{\sigma_b' - u}{\sigma_b'}\right) \cdot 100 \qquad (8)$$

We consider that the normalization of effective stress decrease is less dependent on characteristic features of our study area, such as the depth of the slip surface and aquifer, and hence may be more comparable with studies on other soil slopes worldwide. We color-coded the rainfall events into six different classes of normalized effective stress decrease (c.f. legend in Fig. 7B) and performed the Frequentist method to calibrate a power law function for the beginning of effective stress decrease, being hereafter referred to as effective stress threshold (Eq. 9).

$I = 5.19D^{-0.30}$ (9)

The effective stress threshold and the rainfall threshold by Sidle and Ochiai (2006) separate the rainfall events into three regions (indicated by numbers 1-3 in Fig. 7A). For each region, we quantified classes of effective stress decrease by means of frequency distribution (Inset in Fig. 7A). The first region represents all rainfall events below the effective stress threshold and mostly consists of small rainfall events. The second region encompasses all rainfall events between the effective stress threshold and the rainfall threshold by Sidle and Ochiai (2006). Around 45% of the rainfall events showed effective stress reductions mainly in the lower classes 2 and 3, which correspond to normalized effective stress decreases between 0 and 15%. In the third region, above the threshold by Sidle and Ochiai (2006), most rainfall events (78%) caused effective stress decreases. More than one quarter of rainfall events lie in class 6 accounting for normalized effective stress decreases between 28 and 36%. These rainfall events also include the two large rainfall events that triggered landslides in our study area. The other rainfall events of class 6 exhibit lower rainfall duration, which may be the reason why landslides were not triggered during these events (Wei et al., 2018). A considerable proportion of rainfall events above the effective stress threshold (Regions 2 and 3) did not cause any effective stress decrease. This finding shows that the effective stress threshold is either not always applying to rainfall events recorded since January 2014 or that other factors, such as antecedent precipitation, soil moisture, or locally varying rainfall, may have additionally affected the pore pressure increase in the aquifer at Omokoroa (Rahardjo et al., 2005; Segoni et al., 2018a; Segoni et al., 2018b; Yamao et al., 2016).

6. PREDICTIVE CAPABILITY

We validated the capability of the global rainfall threshold by Sidle and Ochiai (2006) and our new effective stress threshold to predict landslides and the beginning of effective stress, respectively. The two contingency matrices classify rainfall events as either true positives (TP), true negatives (TN), false positives (FP), or false negatives (FN) (Tab. 3). The contingency matrices were used to calculate different skill scores of predictive capabilities (sensitivity, specificity, positive prediction power, negative prediction power).

Both thresholds exhibit sensitivities (Se) and specificities (Sp) close to 1 indicating an overall good predictive capability (Rosi et al., 2015). The positive prediction power (PPP) of the rainfall threshold by Sidle and Ochiai (2006) is low compared to literature (Rosi et al., 2015). This is likely because of the low number of rainfall events that triggered landslides in our study. The positive prediction power of the effective stress threshold lies within the range of other values reported in the literature (Rosi et al., 2015). The probability to correctly predict effective stress decrease is 53%. The negative prediction power of both thresholds is close to 1 indicating that they are well capable to correctly predict rainfall

events that did not trigger landslides or that did not cause any effective stress decrease. The high negative prediction power may also be influenced by the relatively small number of rainfall events used in this study.

For future research we suggest to increase the investigation time period as well as the number and spatial distribution of piezometers within the study area. This would, on the one hand, provide a larger data base for threshold calibration and validation, and on the other, it would prevent local variabilities in the aquifer and moisture conditions of the soil slope to influence the calibration of the effective stress threshold. Furthermore, it has to be tested whether or not the effective stress threshold is also applicable to other soils (e.g. sedimentary clays and sands) and environmental constraints (e.g. dry and tropical) that are significant different to our study area. As Segoni et al. (2018a) pointed out in their recent review, the implementation of pore water pressure into the calibration of rainfall thresholds would add a beneficial perspective. We believe that our effective stress threshold contributes towards the implementation of pore water pressure (and effective stress decrease) into rainfall thresholds.

7. CONCLUSIONS

We have studied a ~40-m-thick succession of altered siliceous pyroclastic deposits dating to c. 0.9 Ma that are dominated by halloysite at Omokoroa peninsula, Tauranga Harbour, the site of multiple landslide events. We show that the trigger mechanism and the landslide dimensions are in keeping with those reported for other landslides in halloysitic tephra deposits from Hong Kong and Japan. The normalized effective stress principle and effective stress threshold developed in our study provide a better understanding of the rainfall triggering of landslides in halloysitic soil materials worldwide. Because the rainfall intensity-duration threshold by Sidle and Ochiai (2006) very well reproduces not only the shallow-translational but also the deep-rotational landslides in our study area, we conclude that the rainfall threshold may be extended to these types of landslides in the future. We also found that:

- Landslides in halloysitic tephras exhibit travel angles between subaerial and submarine landslides reported in other materials and environments worldwide.
- In our study, landslides were triggered when rainfall events exceeded the rainfall threshold of Sidle and Ochiai (2006) as well as the rainfall duration threshold of $D = 24$ proposed by Wei et al. (2018).
- A new effective stress threshold was calibrated based on rainfall events that caused effective stress decrease in the slope. Landslides coincided with rainfall events with highest effective stress decrease.
- The predictive capability of the effective stress threshold is generally satisfactory. The positive prediction power of the threshold could be improved by increasing the number of rainfall events used for the calibration and validation.

ACKNOWLEDGMENTS

This research was funded by the DFG Research Center MARUM of the University of Bremen, Germany, through INTERCOAST and the University of Waikato in Hamilton, New Zealand. We acknowledge the New Zealand Geotechnical Society (NZGS) for funding parts of this project. We thank the Bay of Plenty Regional Council who provided us with the rainfall data from Goodall Road, Whakamarama. Maps in Fig. 1 were created by using a 250-m-resolution national bathymetry grid, provided by NIWA, licensed under NODL By-NN-NC-Sa 1.0, an 8-m-resolution regional digital elevation model, and a 1-m-resolution local LIDAR digital elevation model, both provided by LINZ, licensed under CC BY 4.0. We thank Dirk Immenga, Jimmy Van der Pauw, and Wade Roest for conducting the bathymetric and seismic surveys and Ben Campbell who helped with the field descriptions of the landslides. We gratefully acknowledge Matt Ikari who provided helpful comments on the manuscript. The article is an output of the EXTRAS project "EXTending TephRAS as a global geoscientific research tool stratigraphically, spatially, analytically, and temporally" led by the International focus group on tephrochronology and volcanism (INTAV) of the Stratigraphy and Chronology Commission (SACCOM) of the International Union for Quaternary Research (INQUA) for 2015–2019.

REFERENCE CITED

- Adamo, P., Violante, P., and Wilson, M., 2001, Tubular and spheroidal halloysite in pyroclastic deposits in the area of the Roccamonfina volcano (Southern Italy): Geoderma, v. 99, no. 3, p. 295-316.
- Agostini, A., Tofani, V., Nolesini, T., Gigli, G., Tanteri, L., Rosi, A., Cardellini, S., and Casagli, N., 2014, A new appraisal of the Ancona landslide based on geotechnical investigations and stability modelling: Quarterly journal of engineering geology and hydrogeology, v. 47, no. 1, p. 29-43.
- Askenasy, P., Dixon, J., and McKee, T., 1973, Spheroidal halloysite in a Guatemalan soil: Soil Science Society of America Journal, v. 37, no. 5, p. 799-803.
- Assier-Rzadkieaicz, S., Heinrich, P., Sabatier, P., Savoye, B., and Bourillet, J., 2000, Numerical modelling of a landslide-generated tsunami: the 1979 Nice event: Pure and Applied Geophysics, v. 157, no. 10, p. 1707-1727.
- Basher, L. R., 2013, Erosion processes and their control in New Zealand: Ecosystem services in New Zealand–conditions and trends, v. 2013, p. 363-374.
- Baum, R. L., and Godt, J. W., 2010, Early warning of rainfall-induced shallow landslides and debris flows in the USA: Landslides, v. 7, no. 3, p. 259-272.
- Birrell, K., Fieldes, M., and Williamson, K., 1955, Unusual forms of halloysite: American Mineralogist, v. 40, no. 1-2, p. 122-124.
- Briggs, R., Hall, G., Harmsworth, G., Hollins, A., Houghton, B., Hughes, G., Morgan, M., and Whitbread-Edwards, A., 1996, Geology of the Tauranga area: Department of Earth Sciences, University of Waikato.
- Briggs, R., Houghton, B., McWilliams, M., and Wilson, C., 2005, 40Ar/39Ar ages of silicic volcanic rocks in the Tauranga-Kaimai area, New Zealand: dating the transition between volcanism in the Coromandel Arc and the Taupo Volcanic Zone: New Zealand Journal of Geology and Geophysics, v. 48, no. 3, p. 459-469.
- Brunetti, M., Peruccacci, S., Rossi, M., Luciani, S., Valigi, D., and Guzzetti, F., 2010, Rainfall thresholds for the possible occurrence of landslides in Italy: Natural Hazards and Earth System Sciences, v. 10, no. 3, p. 447-458.

- Caine, N., 1980, The rainfall intensity-duration control of shallow landslides and debris flows: Geografiska annaler: series A, physical geography, v. 62, no. 1-2, p. 23-27.
- Chappell, J., 1975, Upper Quaternary warping and uplift rates in the Bay of Plenty and west coast, North Island, New Zealand: New Zealand journal of geology and geophysics, v. 18, no. 1, p. 129-154.
- Chigira, M., 2014, Geological and geomorphological features of deep-seated catastrophic landslides in tectonically active regions of Asia and implications for hazard mapping: Episodes, v. 37, no. 4, p. 284-294.
- Chigira, M., Nakasuji, A., Fujiwara, S., and Sakagami, M., 2013, Catastrophic landslides of pyroclastics induced by the 2011 off the Pacific coast of Tohoku Earthquake, Earthquake-Induced Landslides, Springer, p. 139-147.
- Chigira, M., and Yokoyama, O., 2005, Weathering profile of non-welded ignimbrite and the water infiltration behavior within it in relation to the generation of shallow landslides: Engineering geology, v. 78, no. 3, p. 187-207.
- Churchman, G. J., and Lowe, D. J., 2012, Alteration, formation, and occurrence of minerals in soils, *in* Huang, P. M., Li, Y., and Sumner, M. E., eds., Handbook of Soil Sciences. Properties and Processes, 2nd edition USA, CRC Press, p. 20.21-20.72.
- Cravero, F., and Churchman, G. J., 2016, The origin of spheroidal halloysites: a review of the literature: Clay Minerals, v. 51, no. 3, p. 417-427.
- Crozier, M., 2005, Multiple-occurrence regional landslide events in New Zealand: hazard management issues: Landslides, v. 2, no. 4, p. 247-256.
- Cruden, D. M., and Varnes, D. J., 1996, Landslides: investigation and mitigation. Chapter 3-Landslide types and processes: Transportation research board special report, no. 247.
- Cunningham, M. J., Lowe, D. J., Wyatt, J. B., Moon, V. G., and Jock Churchman, G., 2016, Discovery of halloysite books in altered silicic Quaternary tephras, northern New Zealand: Clay Minerals, v. 51, no. 3, p. 351-372.
- de Lange, W., 1993, Wave Climate for No. 1 Reach, Port of Tauranga, Tauranga Harbour, Report to the Port of Tauranga Ltd: Hamilton, New Zealand.: Department of Earth Sciences, University of Waikato.
- De Oliveira, M. T., Furtado, S., Formoso, M. L., Eggleton, R. A., and Dani, N., 2007, Coexistence of halloysite and kaolinite: a study on the genesis of kaolin clays of Campo Alegre Basin, Santa Catarina State, Brazil: Anais da Academia Brasileira de Ciências, v. 79, no. 4, p. 665-681.
- Demers, D., Robitaille, D., Locat, P., and Potvin, J., 2014, Inventory of large landslides in sensitive clay in the province of Québec, Canada: preliminary analysis, *in* L'Heureux, J.-S., Locat, A., Leroueil, S., Demers, D., and Locat, J., eds., Landslides in Sensitive Clays: From Geosciences to Risk Management: Dordrecht, Springer Netherlands, p. 77-89.
- Duncan, J. M., Wright, S. G., and Brandon, T. L., 2014, Soil strength and slope stability, John Wiley & Sons.
- Edgers, L., and Karlsrud, K., 1982, Soil flows generated by submarine slides: Case studies and consequences: Nor. Geotech. Inst. Bull, v. 143, p. 1-11.
- Gulliver, C., and Houghton, B., 1980, Omokoroa Point Land Stability Investigation: Tonkin & Taylor.
- Guzzetti, F., Ardizzone, F., Cardinali, M., Rossi, M., and Valigi, D., 2009, Landslide volumes and landslide mobilization rates in Umbria, central Italy: Earth and Planetary Science Letters, v. 279, no. 3-4, p. 222-229.
- Guzzetti, F., Peruccacci, S., Rossi, M., and Stark, C. P., 2007, Rainfall thresholds for the initiation of landslides in central and southern Europe: Meteorology and atmospheric physics, v. 98, no. 3-4, p. 239-267.
- -, 2008, The rainfall intensity–duration control of shallow landslides and debris flows: an update: Landslides, v. 5, no. 1, p. 3-17.
- Hampton, M. A., Lee, H. J., and Locat, J., 1996, Submarine landslides: Reviews of geophysics, v. 34, no. 1, p. 33-59.

- Houghton, B., and Cuthbertson, A., 1989, Sheet T14BD Kaimai; Geological Map of New Zealand 1: 50,000: Dept. Sci. Indus. Res., Wellington, New Zealand.
- Hsu, K. J., 1975, Catastrophic debris streams (sturzstroms) generated by rockfalls: Geological Society of America Bulletin, v. 86, no. 1, p. 129-140.
- Imbert, T., and Desprairies, A., 1987, Neoformation of halloysite on volcanic glass in a marine environment: Clay Minerals, v. 22, no. 2, p. 179-185.
- Irfan, T., 1992, Mineralogical assessment of creep-type instability at two landslip sites: Geotechnical Engineering office.
- -, 1998, Structurally controlled landslides in saprolitic soils in Hong Kong: Geotechnical & Geological Engineering, v. 16, no. 3, p. 215-238.
- Jeong, G., and Kim, S., 1996, Morphology of halloysite particles and aggregates in the weathering of anorthosite: Journal of the Mineralogical Society of Korea, v. 9, p. 64-70.
- Jorat, M. E., Moon, V. G., Hepp, D. A., Kreiter, S., de Lange, W. P., Feldmann, S., and Mörz, T., 2017, Subseafloor investigation of sediments at Southern Tauranga Harbour, New Zealand, before capital dredging: Journal of Coastal Research, v. 33, no. 2, p. 227-242.
- Joussein, E., Petit, S., Churchman, J., Theng, B., Righi, D., and Delvaux, B., 2005, Halloysite clay minerals—a review: Clay Minerals, v. 40, no. 4, p. 383-426.
- Kirk, P., Campbell, S., Fletcher, C., and Merriman, R., 1997, The significance of primary volcanic fabrics and clay distribution in landslides in Hong Kong: Journal of the Geological Society, v. 154, no. 6, p. 1009-1019.
- Kirkman, J., 1977, Possible structure of halloysite disks and cylinders observed in some New Zealand rhyolitic tephras: Clay Minerals, v. 12, p. 199.
- Kluger, M. O., Kreiter, S., Moon, V., Orense, R. P., Mills, P., and Moerz, T., 2018, Undrained cyclic shear behaviour of weathered tephra Géotechnique.
- Kluger, M. O., Moon, V. G., Kreiter, S., Lowe, D. J., Churchman, G., Hepp, D. A., Seibel, D., Jorat, M. E., and Mörz, T., 2017, A new attraction-detachment model for explaining flow sliding in clay-rich tephras: Geology, v. 42, no. 2, p. 131-134.
- Kvalstad, T. J., Andresen, L., Forsberg, C. F., Berg, K., Bryn, P., and Wangen, M., 2005, The Storegga slide: evaluation of triggering sources and slide mechanics: Marine and Petroleum Geology, v. 22, no. 1, p. 245-256.
- L'Heureux, J.-S., Eilertsen, R. S., Glimsdal, S., Issler, D., Solberg, I.-L., and Harbitz, C. B., 2012, The 1978 quick clay landslide at Rissa, mid Norway: subaqueous morphology and tsunami simulations, Submarine mass movements and their consequences, Springer, p. 507-516.
- L'Heureux, J.-S., Locat, A., Leroueil, S., Demers, D., and Locat, J., 2014, Landslides in Sensitive Clays–From Geosciences to Risk Management, Landslides in Sensitive Clays, Springer, p. 1-12.
- Labuz, J. F., and Zang, A., 2012, Mohr–Coulomb failure criterion: Rock mechanics and rock engineering, v. 45, no. 6, p. 975-979.
- Larsen, I. J., Montgomery, D. R., and Korup, O., 2010, Landslide erosion controlled by hillslope material: Nature Geoscience, v. 3, no. 4, p. 247.
- Longva, O., Janbu, N., Blikra, L., and Bøe, R., 2003, The 1996 Finneidfjord slide; seafloor failure and slide dynamics, Submarine Mass movements and their consequences, Springer, p. 531-538.
- Loughnan, F., and Roberts, F. I., 1981, The natural conversion of ordered kaolinite to halloysite (1 at Burning Mountain near Wingen'New South Wales: American Mineralogist, v. 66, p. 997-1005.
- Lowe, D. J., 2011, Tephrochronology and its application: a review: Quaternary Geochronology, v. 6, no. 2, p. 107-153.
- Malamud, B. D., Turcotte, D. L., Guzzetti, F., and Reichenbach, P., 2004, Landslides, earthquakes, and erosion: Earth and Planetary Science Letters, v. 229, no. 1-2, p. 45-59.

- Martelloni, G., Segoni, S., Fanti, R., and Catani, F., 2012, Rainfall thresholds for the forecasting of landslide occurrence at regional scale: Landslides, v. 9, no. 4, p. 485-495.
- Moon, V., de Lange, W., Garae, C., Mörz, T., Jorat, M., and Kreiter, S., 2015a, Monitoring the landslide at Bramley Drive, Tauranga, NZ.
- Moon, V. G., Lowe, D. J., Cunningham, M. J., Wyatt, J. B., de Lange, W. P., Churchman, G. J., Mörz, T., Kreiter, S., Kluger, M. O., and Jorat, M. E., Sensitive pyroclastic-derived halloysitic soils in northern New Zealand: Interplay of microstructure, minerals, and geomechanics, *in* Proceedings Volcanic Rocks and Soils2015b, Taylor and Francis, London, p. 3-21.
- Napolitano, E., Fusco, F., Baum, R. L., Godt, J. W., and De Vita, P., 2016, Effect of antecedent-hydrological conditions on rainfall triggering of debris flows in ash-fall pyroclastic mantled slopes of Campania (southern Italy): Landslides, v. 13, no. 5, p. 967-983.
- Nicoletti, P. G., and Sorriso-Valvo, M., 1991, Geomorphic controls of the shape and mobility of rock avalanches: Geological Society of America Bulletin, v. 103, no. 10, p. 1365-1373.
- Norsk Geoteknisk Forening, 1974, Retningslinjer for presentasjon av geotekniske undersökelser: Oslo, Norway, v. 16.
- Parham, W. E., 1970, SP-10 Clay Mineralogy and Geology of Minnesota's Kaolin Clays.
- Parry, S., Campbell, S., and Churchman, G., Kaolin-Rich Zones In Hong Kong Saprolites Their Interpretation And Engineering Significance, *in* Proceedings ISRM International Symposium2000, International Society for Rock Mechanics.
- -, 2001, The origin and shear strength of kaolin-rich zones in Hong Kong: Geotech. Engn, p. 893-897.
- Peruccacci, S., Brunetti, M. T., Luciani, S., Vennari, C., and Guzzetti, F., 2012, Lithological and seasonal control on rainfall thresholds for the possible initiation of landslides in central Italy: Geomorphology, v. 139, p. 79-90.
- Pouclet, A., Cambray, H., Cadet, J.-P., Bourgois, J., and De Wever, P., 28. VOLCANIC ASH FROM LEG 112 OFF PERU1, *in* Proceedings Proceedings of the Ocean Drilling Program: Scientific results1990, The Program, p. 465.
- Quantin, P., and Rambaud, D., 1987, Genesis of spherical halloysite from basaltic ash, at Ambrym (Vanuatu).
- Quayle, A., 1984, The climate and weather of the Bay of Plenty region, Ministry of Transport, New Zealand Meteorological Service.
- Rahardjo, H., Lee, T., Leong, E. C., and Rezaur, R., 2005, Response of a residual soil slope to rainfall: Canadian Geotechnical Journal, v. 42, no. 2, p. 340-351.
- Romero, R., Robert, M., Elsass, F., and Garcia, C., 1992, Abundance of halloysite neoformation in soils developed from crystalline rocks. Contribution of transmission electron microscopy: Clay Minerals, v. 27, no. 1, p. 35-46.
- Rosi, A., Lagomarsino, D., Rossi, G., Segoni, S., Battistini, A., and Casagli, N., 2015, Updating EWS rainfall thresholds for the triggering of landslides: Natural Hazards, v. 78, no. 1, p. 297-308.
- Rösner, A., 2016, Impact of seismicity on Nice's slope stability [M.Sc.: University of Bremen.
- Saigusa, M., Shoji, S., and Kato, T., 1978, Origin and nature of halloysite in Ando soils from Towada tephra, Japan: Geoderma, v. 20, no. 2, p. 115-129.
- Scheidegger, A. E., 1973, On the prediction of the reach and velocity of catastrophic landslides: Rock Mechanics and Rock Engineering, v. 5, no. 4, p. 231-236.
- Segoni, S., Piciullo, L., and Gariano, S. L., 2018a, A review of the recent literature on rainfall thresholds for landslide occurrence: Landslides, v. 15, no. 8, p. 1483-1501.
- Segoni, S., Rosi, A., Lagomarsino, D., Fanti, R., and Casagli, N., 2018b, Brief communication: Using averaged soil moisture estimates to improve the performances of a regional-scale landslide early warning system: Natural Hazards and Earth System Sciences, v. 18, no. 3, p. 807-812.

- Shaller, P., Sykora, D., Doroudian, M., and Churchman, G. J., 2016, Rapid in situ conversion of late-stage volcanic materials to halloysite implicated in catastrophic dam failure, Hawaii: Clay Minerals, v. 51, no. 3, p. 499-515.
- Shepherd, M., Betts, H., McFadgen, B., and Sutton, D., 2000, Geomorphological evidence for a Pleistocene barrier at Matakana Island, Bay of Plenty, New Zealand: New Zealand Journal of Geology and Geophysics, v. 43, no. 4, p. 579-586.
- Sidle, R. C., and Ochiai, H., 2006, Landslides: processes, prediction, and land use, Washington, DC, American Geophysical Union, Water resources monograph series.
- Sieffermann, G., and Millot, G., Equatorial and tropical weathering of recent basalts from Cameroon: allophanes, halloysite, metahalloysite, kaolinite and gibbsite, *in* Proceedings Proceedings of the International Clay Conference, Tokyo1969, Volume 1, Israel University Press, Jerusalem, p. 417-430.
- Singer, A., Zarei, M., Lange, F., and Stahr, K., 2004, Halloysite characteristics and formation in the northern Golan Heights: Geoderma, v. 123, no. 3, p. 279-295.
- Skempton, A., and Northey, R., 1952, The sensitivity of clays: Geotechnique, v. 3, no. 1, p. 30-53.
- Smalley, I., Ross, C. W., and Whitton, J., 1980, Clays from New Zealand support the inactive particle theory of soil sensitivity: Nature, v. 288, p. 576-577.
- Tanaka, K., 1992, Slope hazards and clay minerals: Nendo Kagaku, v. 32, no. 1, p. 16-22.
- Taskey, R. D., 1977, Relationships of clay mineralogy to landscape stability in Western Oregon.
- Tiranti, D., and Rabuffetti, D., 2010, Estimation of rainfall thresholds triggering shallow landslides for an operational warning system implementation: Landslides, v. 7, no. 4, p. 471-481.
- Varnes, D. J., 1978, Slope movement types and processes: Special report, v. 176, p. 11-33.
- Wada, K., and Kakuto, Y., 1985, Embryonic halloysites in Ecuadorian soils derived from volcanic ash: Soil Science Society of America Journal, v. 49, no. 5, p. 1309-1318.
- Wang, G., Suemine, A., Zhang, F., Hata, Y., Fukuoka, H., and Kamai, T., 2014, Some fluidized landslides triggered by the 2011 Tohoku Earthquake (M w 9.0), Japan: Geomorphology, v. 208, p. 11-21.
- Wei, L.-W., Huang, C.-M., Chen, H., Lee, C.-T., Chi, C.-C., and Chiu, C.-L., 2018, Adopting the I 3-R 24 rainfall index and landslide susceptibility for the establishment of an early warning model for rainfall-induced shallow landslides: Natural Hazards & Earth System Sciences, v. 18, no. 6.
- Wen, B., and Aydin, A., 2003, Microstructural study of a natural slip zone: quantification and deformation history: Engineering Geology, v. 68, no. 3, p. 289-317.
- Yamao, M., Sidle, R., Gomi, T., and Imaizumi, F., 2016, Characteristics of landslides in unwelded pyroclastic flow deposits, southern Kyushu, Japan: Natural Hazards and Earth System Sciences, v. 16, no. 2, p. 617-627.
- Zaruba, Q., and Mencl, V., 2014, Landslides and their control, Elsevier.

FIGURE CAPTIONS

Fig. 1. Study area. A: Distribution coastal landslides along the northwest coast of Omokoroa. The topographic map is overlain by landslide main scarps, landslide dimensions, and bathymetry data from the near shore area. **B:** Location of Omokoroa peninsula within the estuarine lagoon of Tauranga Harbour, northern New Zealand. **C-E:** Photographs of coastal landslides at Omokoroa. The locations are indicated in Fig. 1A.

Fig. 2. Geology of the 1979 Bramley Drive landslide. A: Stratigraphy of the succession of lignite, ignimbrite, and tephra-fall deposits, and intervening paleosols (P). **B:** Relative concentrations of different halloysite clay morphologies with depth after Kluger et al. (2017). **C:** Cross-section of the 1979 Bramley Drive landslide showing the locations of the confined and unconfined aquifers, respectively, with locations of upper (U), middle (M), and lower (L) piezometers. Upper and lower tidal ranges are from de Lange (1993). **D:** Scanning electron microscope images of mushroom cap-shaped spheroidal halloysite, abundant in the highly sensitive layer within the Pahoia Tephras. The images are modified with permission from Kluger et al. (2017), copyright 2017 The Geological Society of America.

Fig. 3 Pore water pressure (PWP) and rainfall characteristics. A-B: PWP and hourly rainfall time series from January 2014 to June 2018. Green circles indicate large rainfall events having been taken from rain gauges at the Bramley Drive landslide (dark green) or at Goodall Road, Whakamarama (light green). **C-D:** Rainfall correlations between rain gauges at Bramley Drive landslide and Goodall Road, Whakamarama. **E:** Hourly rainfall, PWP, and number of recent landslides during the 2017 cyclone season.

Fig. 4. Landslide dimensions. r^2 is the coefficient of determination.

Fig. 5. Sedimentary architecture of the subtidal area, northwest Omokoroa. A: Along-shore and **B:** cross-shore seismic profiles and interpretation of seismic units.

Fig. 6. Effect of rainfall events on effective stress decrease. Changes in water table and effective stress in the soil slope of the Bramley Drive landslide with **A:** rainfall intensity and **B:** duration of rainfall events. The length of arrows indicates the change in water table and effective stress, respectively. The colors of the arrows represent the increase in water table as defined in the color scale.

Fig. 7. Rainfall thresholds Rainfall intensity-duration relationships of small and large rainfall events plotted on **A:** logarithmic and **B:** linear scales. The two large rainfall events that triggered landslides at Omokoroa are well constraint by considering the two thresholds proposed by Caine (1980) and Wei et

al. (2018). The effective stress threshold is the lower bound of large rainfall events at the 5 % confidence interval. The colors of symbols and of the stacked bar chart are defined in the legend of Fig. 7B.

TABLE

Tab 1. Coastal landslides at Omokoroa peninsula, Tauranga Harbour, New Zealand.

Landslide No.	Location	Material composition	Type	Landslide dimension										Timing
				D_r	W_r	L_r	H	L	A_L	V_T	V_r	H/L	β	
				m	m	m	m	m	m^2	m^3	m^3		°	
L-1	Waterview Ter	TPI, PT*,	D^S	7	25	25	20	30	625		2,291	0.67	34	A
L-2	Hamurana Rd – Kaharoa Av	TPI*, PT	S		185	6	5	8	1,185	1,811		0.67	34	A
L-3-1		TPI	S		30	32	20	50	960	1,370		0.40	22	A
L-3-2		TPI*, PT	D	5.5	15	14	10	20	212		611	0.50	27	A
L-3-3		PT	S		5	10	7	10	49	26		0.70	35	A
L-4	Kaharoa Av	N/A	D^S	4	15	16	10	12	234		491	0.83	40	A
L-5	Kowai Grv	TPI, PT*,	D	9	30	32	20	38	960		4,526	0.53	28	A
L-6		TPI	S		29	29	20	21	841	1,148		0.95	44	A
L-7	McDonnell St	N/A	S		20	25	15	25	500	574		0.60	31	A
L-8		TPI	S		48	9	8	5	410	441		1.60	58	A
L-9		TPI, PT*,	D^S	14	25	58	30	115	1,458		10,686	0.26	15	A
L-10	Bramley Dr	PT, HA	S		64	36	30	30	2,308	4,403		1.00	45	A
L-11		PT, HA	D	27	62	68	32	210	4,216		59,602	0.15	9	1979†
L-12		PT, HA	S		10	17	15	15	170	136		1.00	45	A‡, B
L-13	Ruamoana Pl	PT, HA	S		14	25	21	25	343	348		0.85	41	A
L-14		PT	D	6	19	15	9	30	278		872	0.30	17	B
L-15		PT	D	7	15	15	9	30	225		825	0.30	17	B
L-16	Myrtle Dr	TPI*, PT	D	4	14	17	8	25	235		491	0.32	18	A‡, B
L-17		TPI	S		15	9	8	10	142	107		0.80	39	A
L-18		TPI	S		30	18	15	20	541	637		0.75	37	B
L-19	Crapp Historic Reserve	TPI, PT, HA	S		35	14	14	10	484	550		1.35	53	A
L-20		TPI, PT, HA	S		7	20	20	10	142	107		2.00	63	A
L-21		TPI, PT, HA	S		25	12	12	10	309	303		1.20	50	A
L-22		TPI, PT, HA	S		15	11	10	20	168	134		0.50	27	A
L-23		TPI, PT, HA	S		8	13	13	7	107	73		1.86	62	A
L-24		TPI, PT, HA	S		11	14	14	6	152	118		2.25	66	A
L-25		TPI, PT, HA	S		21	12	10	10	257	236		0.95	44	A
L-26	Harbour View Rd	TPI	D^S	6	20	28	19	50	552		1,733	0.38	21	A

*Base of slide surface
†1979 Bramley Drive landslide dimensions from Gulliver and Houghton (1980)
‡Main failure event
Ter–Terrace; Rd–Road; Av–Avenue; Grv–Grove; St–Street; Dr–Drive; Pl–Place
TPI–Te Puna Ignimbrite; PT–Pahoia Tephras; HA–Hamilton Ashes; N/A–Not available
D–deep-seated; S–shallow; D^S–complex earth slide with deep-seated being the dominant mode of failure and shallow failure associated to the main event
A–Cyclone Debbie (April 5th, 2017); B–Cyclone Cook (April 13th, 2017); Years in CE (Common era)

Tab. 2. Definitions of predictive capability variables.

Variable	Name	Description
TP	True positives	Threshold exceeded; landslide(s)/effective stress decrease occurred
TN	True negatives	Threshold not exceeded; landslide(s)/effective stress decrease did not occur
FP	False positives	Threshold exceeded; landslide(s)/effective stress decrease did not occur
FN	False negatives	Threshold not exceeded; landslide(s)/effective stress decrease occurred
$Se = \frac{TP}{TP+FN}$	Sensitivity	Ability to properly classify rainfalls that caused landslide(s)/effective stress decrease
$Sp = \frac{TN}{TN+FP}$	Specificity	Ability to properly classify rainfalls that did not cause landslide(s)/effective stress decrease
$PPP = \frac{TP}{FP+TP}$	Positive prediction power	Probability of correctly classifying a rainfall that caused landslide(s)/effective stress decrease
$NPP = \frac{TN}{TN+FN}$	Negative prediction power	Probability of correctly classifying a rainfall that did not cause landslide(s)/effective stress decrease

Tab. 3. Variables of predictive capability for the rainfall thresholds considered in this study.

Threshold	Aim	TP	TN	FP	FN	Se	Sp	PPP	NPP
Sidle and Ochiai (2006)	Landslide occurrence	2	798	34	0	1.000	0.959	0.056	1.000
Effective stress threshold	Beginning of effective stress decrease	40	739	36	1	0.976	0.954	0.526	0.999

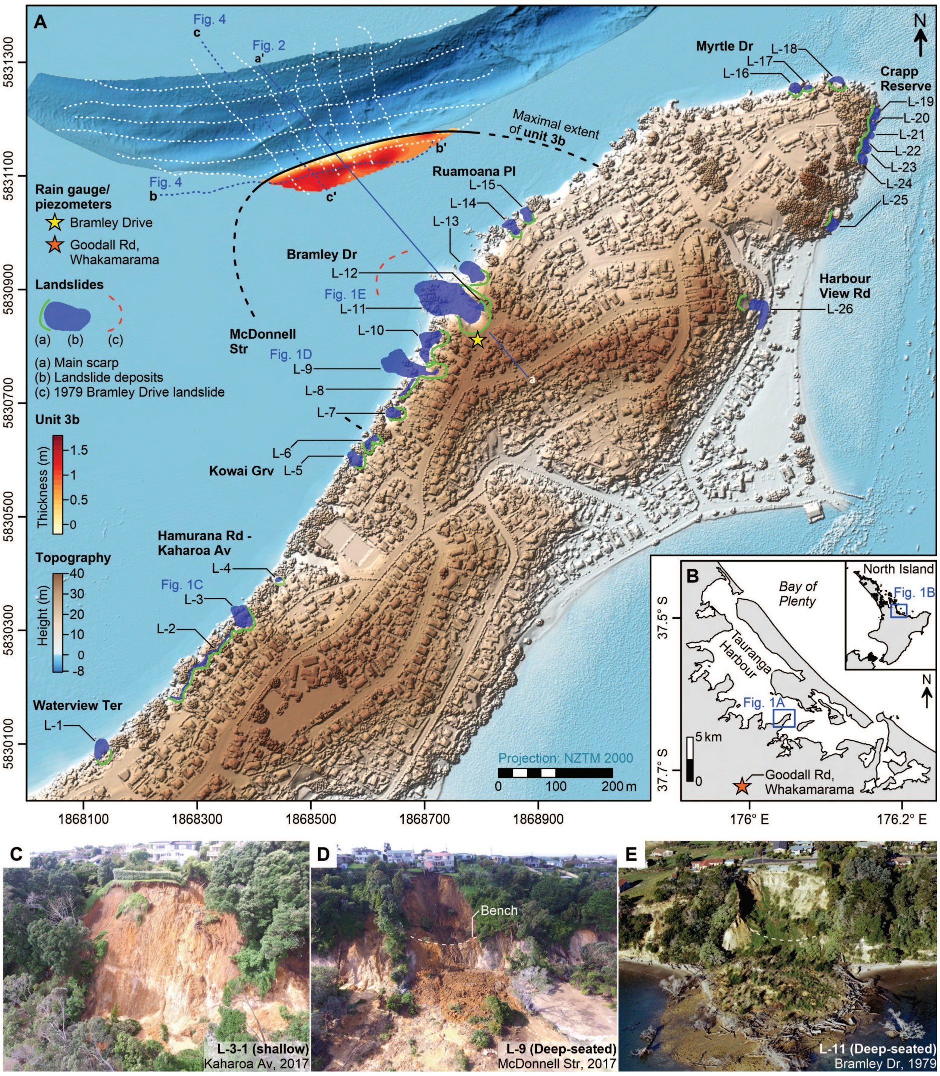
A
Fig. 4
c
Fig. 2
a'
Maximal extent of unit 3b
b'
c'
Fig. 4
b
Myrtle Dr
L-16
L-17
L-18
Crapp Reserve
L-19
L-20
L-21
L-22
L-23
L-24
L-25
Ruamoana Pl
L-15
L-14
L-13
Bramley Dr
L-12
Fig. 1E
L-11
L-10
Fig. 1D
L-9
L-8
L-7
L-6
L-5
Kowai Grv
McDonnell Str
Harbour View Rd
L-26
Rain gauge/ piezometers
Bramley Drive
Goodall Rd, Whakamarama
Landslides
(a) (b) (c)
(a) Main scarp
(b) Landslide deposits
(c) 1979 Bramley Drive landslide
Unit 3b
Thickness (m)
1.5
1
0.5
0
Topography
Height (m)
40
30
20
10
0
-8
Hamurana Rd - Kaharoa Av
L-4
Fig. 1C
L-3
L-2
Waterview Ter
L-1
Projection: NZTM 2000
0 100 200 m
5831300
5831100
5830900
5830700
5830500
5830300
5830100
1868100
1868300
1868500
1868700
1868900
B
Bay of Plenty
North Island
Fig. 1B
Tauranga Harbour
Fig. 1A
5 km
0
Goodall Rd, Whakamarama
37.5° S
37.7° S
176° E
176.2° E
N
C
L-3-1 (shallow)
Kaharoa Av, 2017
D
Bench
L-9 (Deep-seated)
McDonnell Str, 2017
E
L-11 (Deep-seated)
Bramley Dr, 1979

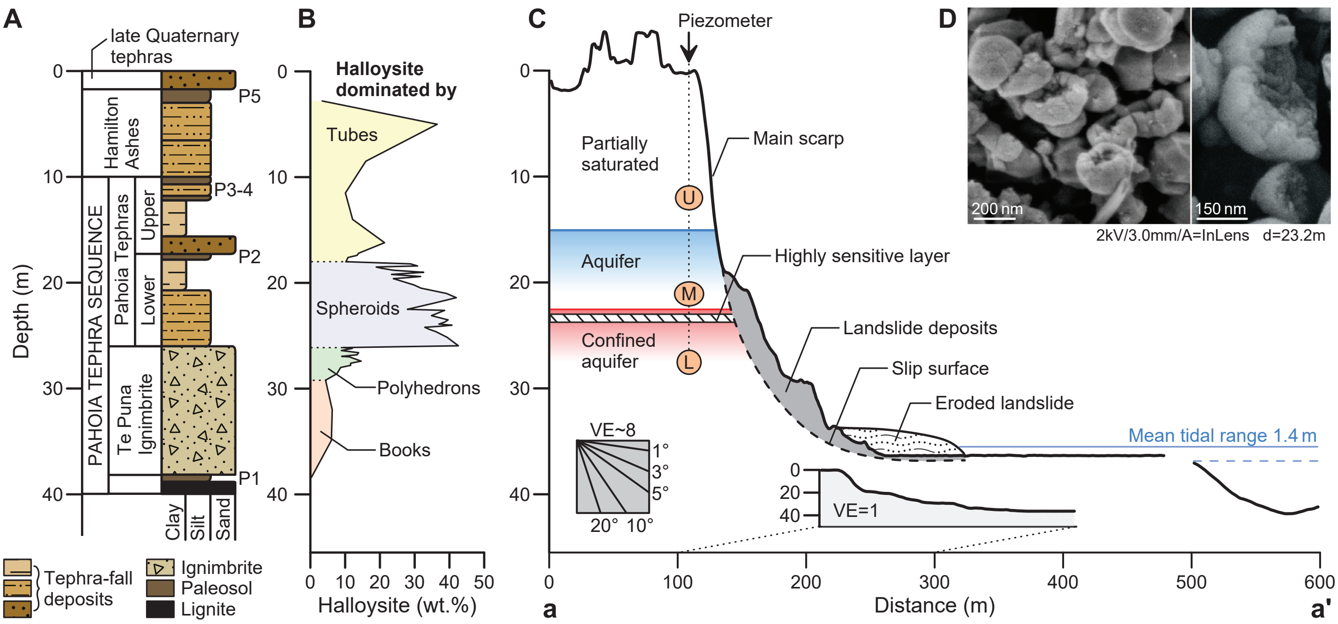
A
late Quaternary tephras
Depth (m)
0
10
20
30
40
Hamilton Ashes
PAHOIA TEPHRA SEQUENCE
Pahoia Tephras
Upper
Lower
Te Puna Ignimbrite
P5
P3-4
P2
P1
Clay
Silt
Sand
Tephra-fall deposits
Ignimbrite
Paleosol
Lignite
B
Halloysite dominated by
Tubes
Spheroids
Polyhedrons
Books
0 10 20 30 40 50
Halloysite (wt.%)
C
Piezometer
Partially saturated
Main scarp
U
Aquifer
Highly sensitive layer
M
Confined aquifer
L
Landslide deposits
Slip surface
Eroded landslide
Mean tidal range 1.4 m
VE~8
1°
3°
5°
20°
10°
VE=1
0
100
200
300
400
500
600
Distance (m)
a
a'
D
200 nm
150 nm
2kV/3.0mm/A=InLens d=23.2m

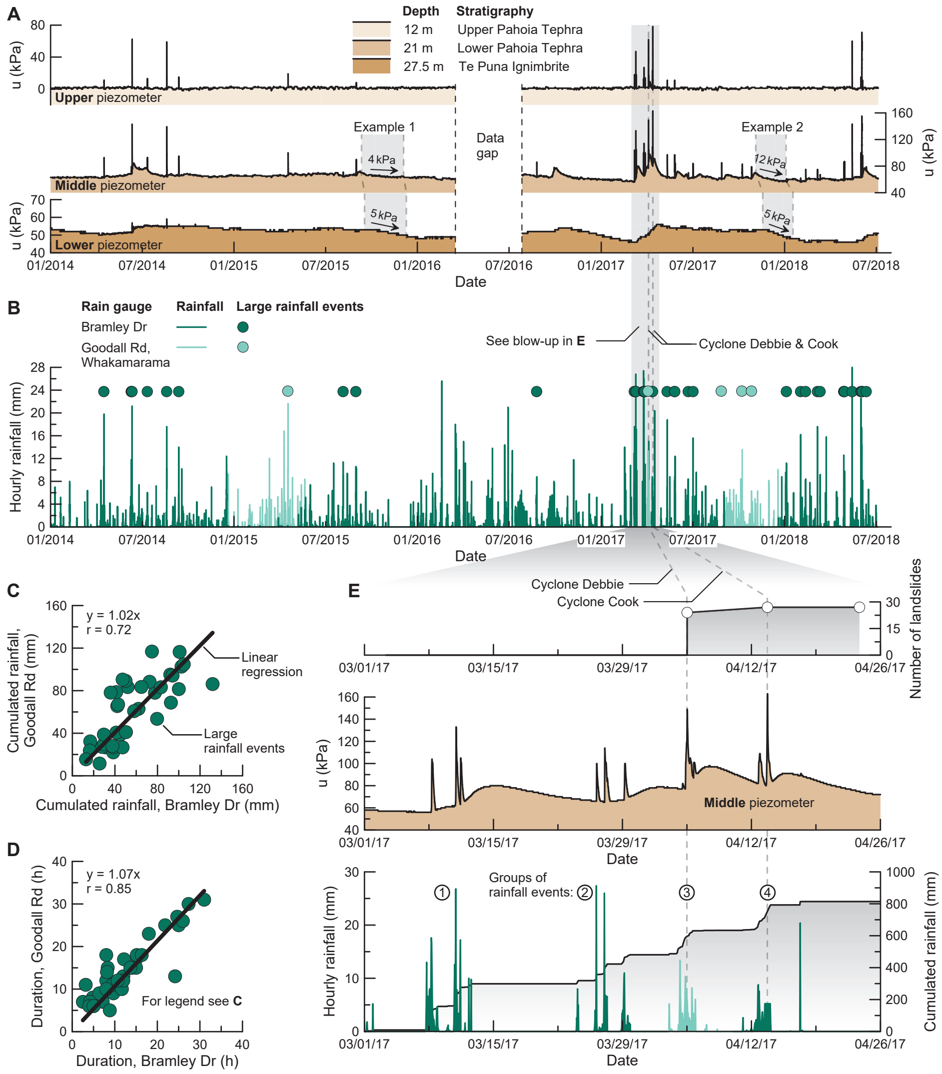

A
Depth Stratigraphy
12 m Upper Pahoia Tephra
21 m Lower Pahoia Tephra
27.5 m Te Puna Ignimbrite
Upper piezometer
Middle piezometer
Lower piezometer
Example 1
Example 2
Data gap
4 kPa
12 kPa
5 kPa
5 kPa
u (kPa)
Date
B
Rain gauge
Rainfall
Large rainfall events
Bramley Dr
Goodall Rd, Whakamarama
See blow-up in E
Cyclone Debbie & Cook
Hourly rainfall (mm)
Date
C
y = 1.02x
r = 0.72
Linear regression
Large rainfall events
Cumulated rainfall, Goodall Rd (mm)
Cumulated rainfall, Bramley Dr (mm)
D
y = 1.07x
r = 0.85
For legend see C
Duration, Goodall Rd (h)
Duration, Bramley Dr (h)
E
Cyclone Debbie
Cyclone Cook
Number of landslides
Middle piezometer
u (kPa)
Date
Groups of rainfall events: ① ② ③ ④
Hourly rainfall (mm)
Cumulated rainfall (mm)
Date

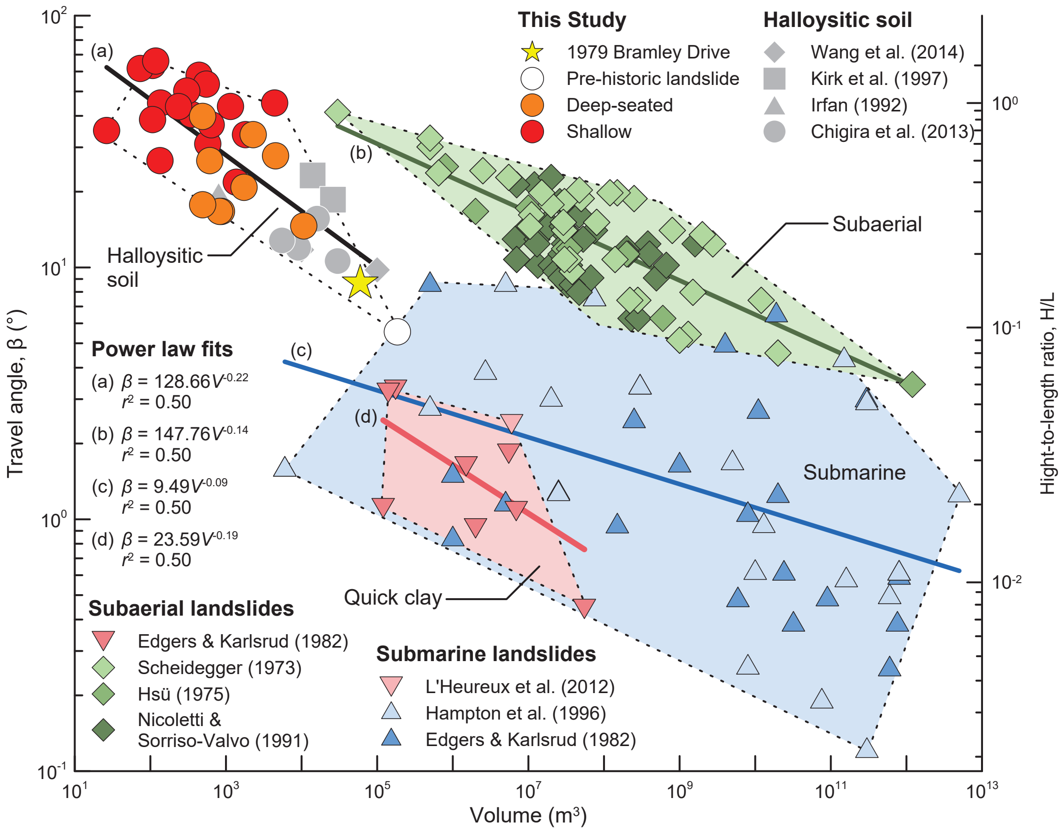

This Study
1979 Bramley Drive
Pre-historic landslide
Deep-seated
Shallow
Halloysitic soil
Wang et al. (2014)
Kirk et al. (1997)
Irfan (1992)
Chigira et al. (2013)
Subaerial
Submarine
Quick clay
Power law fits
(a) $\beta = 128.66V^{-0.22}$ $r^2 = 0.50$
(b) $\beta = 147.76V^{-0.14}$ $r^2 = 0.50$
(c) $\beta = 9.49V^{-0.09}$ $r^2 = 0.50$
(d) $\beta = 23.59V^{-0.19}$ $r^2 = 0.50$
Subaerial landslides
Edgers & Karlsrud (1982)
Scheidegger (1973)
Hsü (1975)
Nicoletti & Sorriso-Valvo (1991)
Submarine landslides
L'Heureux et al. (2012)
Hampton et al. (1996)
Edgers & Karlsrud (1982)
Travel angle, β (°)
Hight-to-length ratio, H/L
Volume (m³)

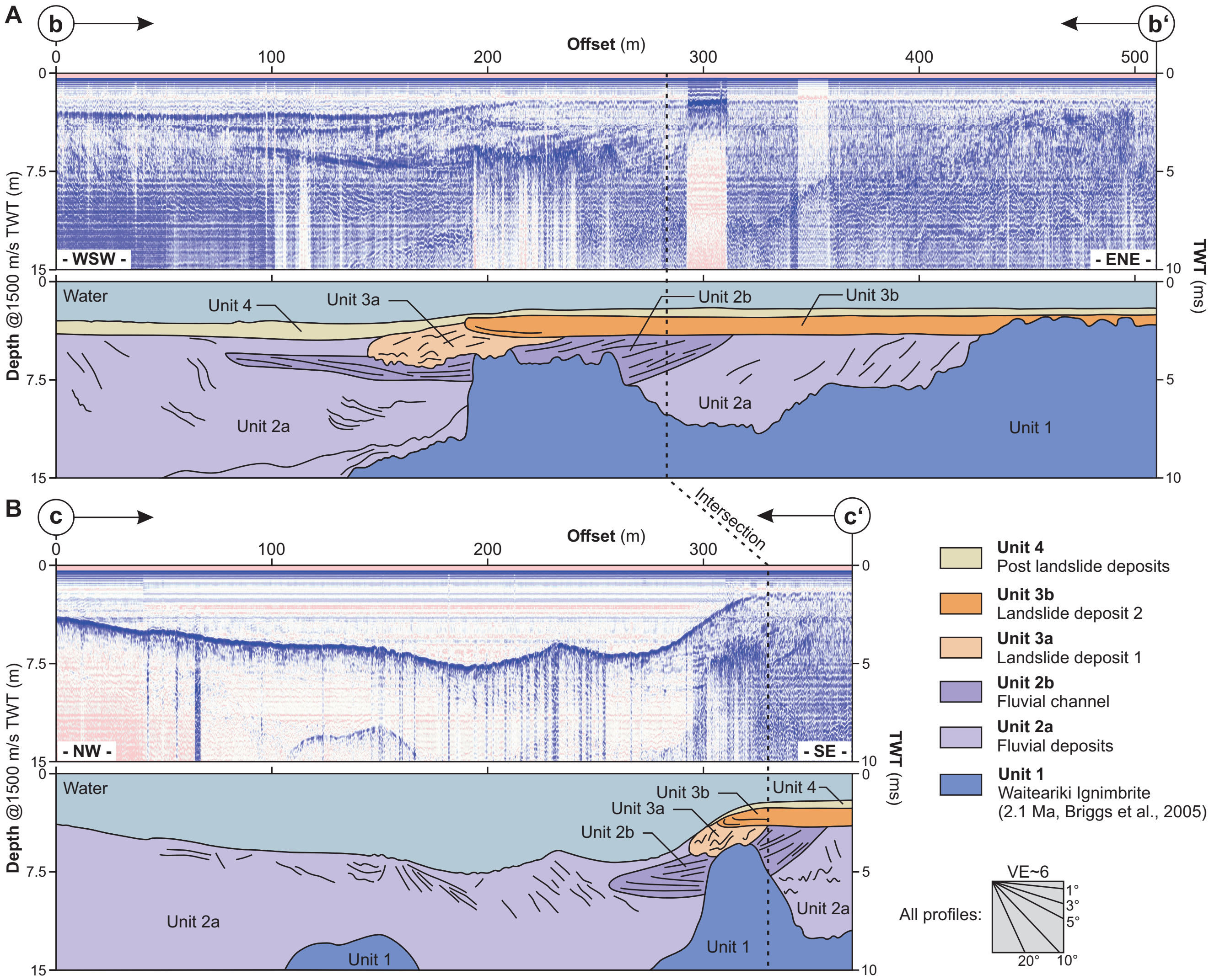
A
b
b'
Offset (m)
0
100
200
300
400
500
- WSW -
- ENE -
Depth @1500 m/s TWT (m)
TWT (ms)
Water
Unit 4
Unit 3a
Unit 2b
Unit 3b
Unit 2a
Unit 1
Intersection
B
c
c'
- NW -
- SE -
Unit 4
Post landslide deposits
Unit 3b
Landslide deposit 2
Unit 3a
Landslide deposit 1
Unit 2b
Fluvial channel
Unit 2a
Fluvial deposits
Unit 1
Waiteariki Ignimbrite
(2.1 Ma, Briggs et al., 2005)
VE~6
All profiles:
1°
3°
5°
20°
10°

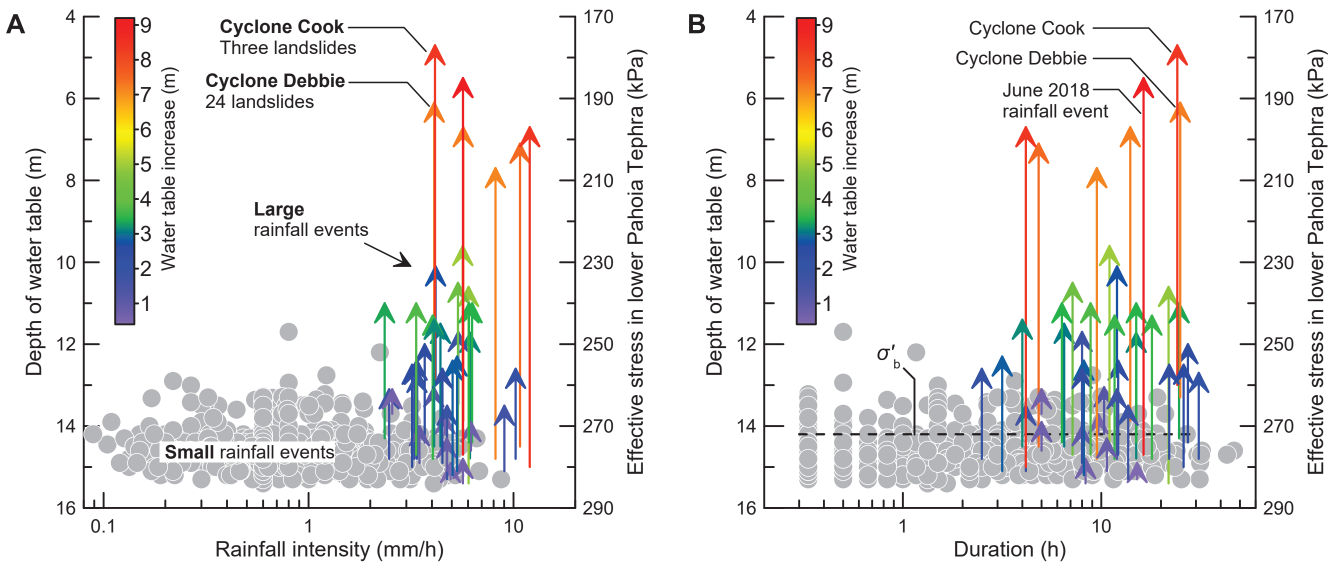
A
Cyclone Cook
Three landslides
Cyclone Debbie
24 landslides
Large
rainfall events
Small rainfall events
Depth of water table (m)
Water table increase (m)
Effective stress in lower Pahoia Tephra (kPa)
Rainfall intensity (mm/h)
B
Cyclone Cook
Cyclone Debbie
June 2018
rainfall event
σ'b
Duration (h)

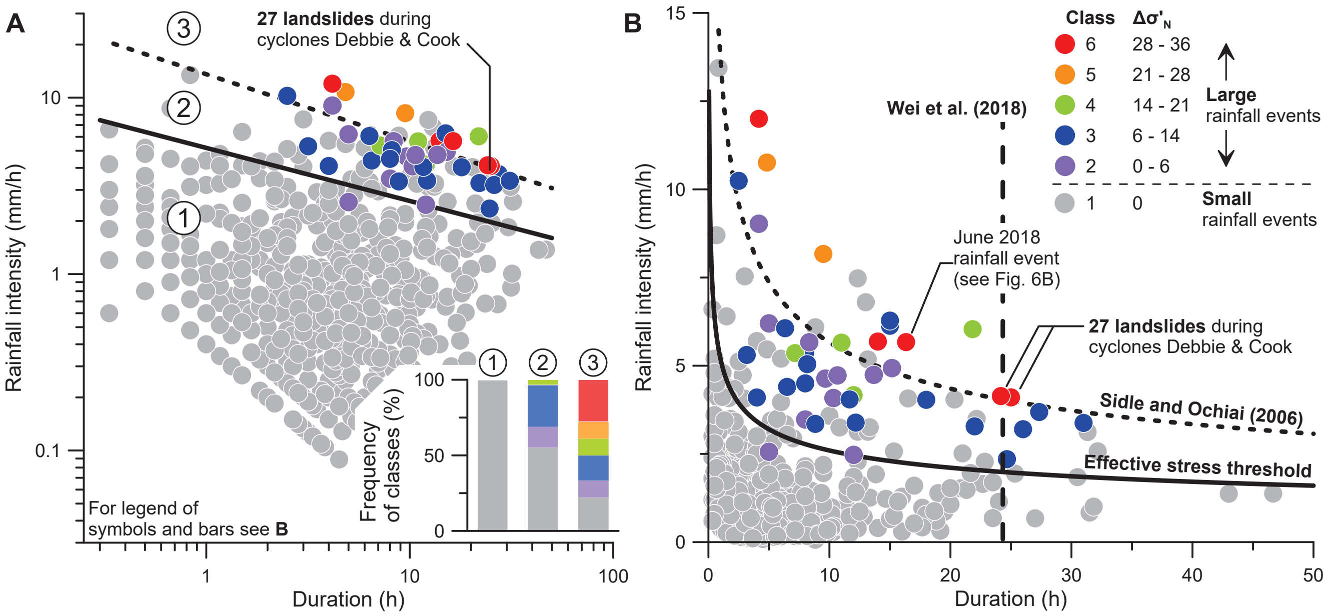

A
B
27 landslides during cyclones Debbie & Cook
Rainfall intensity (mm/h)
Duration (h)
For legend of symbols and bars see B
Frequency of classes (%)
Class
Δσ'N
Large rainfall events
Small rainfall events
Wei et al. (2018)
June 2018 rainfall event (see Fig. 6B)
Sidle and Ochiai (2006)
Effective stress threshold